The International Journal of Advanced Manufacturing Technology (2024) 132:1111–1125
https://doi.org/10.1007/s00170-024-13378-1

ORIGINAL ARTICLE

Numerical modeling of fill-level and residence time in starve-fed single-screw extrusion: a dimensionality reduction study from a 3D CFD model to a 2D convection-diffusion model

Erik Holmen Olofsson[1] · Ashley Dan[2] · Michael Roland[1] · Ninna Halberg Jokil[3] · Rohit Ramachandran[2] · Jesper Henri Hattel[1]

Received: 8 November 2023 / Accepted: 29 February 2024 / Published online: 19 March 2024

Abstract
This research delves into the numerical predictions of fill-level and residence time distribution (RTD) in starve-fed single-screw extrusion systems. Starve-feeding, predominantly used in ceramic extrusion, introduces challenges which this study seeks to address. Based on a physical industrial system, a comprehensive 3D computational fluid dynamics (CFD) model was developed using a porous media representation of the complex multi-hole plate die. Validations performed using real sensor data, accounting for partial wear on auger screw flights, show an ~11% discrepancy without accounting for screw wear and ~6% when considering it. A 2D convection-diffusion model was introduced as a dimensionality reduced order model (ROM) with the intention of bridging the gap between comprehensive CFD simulations and real-time applications. Central to this model's prediction ability was both the velocity field transfer from the CFD model and calibration of the ROM diffusion coefficient such that a precise agreement of residence time distribution (RTD) curves could be obtained. Some discrepancies between the CFD and the ROM were observed, attributed to the loss of physical information of the system when transitioning from a higher fidelity CFD model to a semi-mechanistic ROM and the inherent complexities of the starved flow in the compression zone of the extruder. This research offers a comprehensive methodology and insights into reduced order modeling of starve-fed extrusion systems, presenting opportunities for real-time optimization and enhanced process understanding.

Keywords Reduced order model · Numerical simulation · CFD · Starve-fed extrusion · Metamodeling · Catalyst manufacturing

1 Introduction

Extruders are most often operated with the screw fully filled (flood-fed). However, in ceramic extrusion [1], starve-feeding is often used to eliminate problems with bridging and funneling in the feed hopper or slippage on the barrel in the extruder. Starve feeding results in a partially filled section of the screw, and the pressure starts to build from the point where the screw becomes fully filled [2]. The distance from this point to the end of the screw defines the extruder filling degree and is referred to as the extruder "fill length" (L_{fill}) [3]. Although some models exist for theoretically approximating L_{fill}, application of these models is typically very difficult due to complex geometries and fluid rheology [3].

✉ Erik Holmen Olofsson
ethol@dtu.dk

Ashley Dan
ashley.dan@rutgers.edu

Michael Roland
mirola@dtu.dk

Ninna Halberg Jokil
nih@topsoe.com

Rohit Ramachandran
rohitrr@soe.rutgers.edu

Jesper Henri Hattel
jhat@dtu.dk

[1] Department of Mechanical Engineering, Technical University of Denmark, Kgs. Lyngby, Denmark

[2] Department of Chemical & Biochemical Engineering, Rutgers, The State University of New Jersey, New Brunswick, NJ, USA

[3] R&D Director – Topsoe A/S, Haldor Topsøes Allé 1, DK-2800, Kgs, Lyngby, Denmark

Therefore, the modeling of starve fed single-screw extrusion is quite limited [4]. Ensuring a sufficient and stable increased degree of fill can, however, reduce the amount of over-processing, promoting better and more consistent product quality [5]. Another quantity relevant for providing insights into the mixing, reaction kinetics, and overall system behavior is the residence time distribution (RTD) [6]. RTD refers to the distribution of time that particles or fluid elements spend within a specific process or reactor, and its consideration is crucial for any process engineering undertaking, encompassing flow processes [7, 8]. Understanding the RTD involves using mathematical models, tracer studies, and computational simulations [9–11]. Tracer studies involve introducing a non-reactive substance, called a tracer, into the extrusion process and tracking its behavior through the system. This allows the collection of data that can be used to construct an RTD curve.

In the realm of complex systems and simulations, obtaining accurate and real-time results often comes at the cost of computational resources and time. Systems governed by intricate physical, mathematical, or engineering principles can lead to high-dimensional models that are computationally expensive to solve or simulate. This is where reduced order modeling (ROM) emerges as a crucial technique [12, 13]. ROM is a methodology aimed at representing complex, high-dimensional systems with a much smaller set of variables, allowing for efficient simulations, optimizations, and analyses without significant loss of accuracy. The primary motivation behind ROM lies in striking a balance between accuracy and computational efficiency. Many real-world systems, such as fluid dynamics in engineering applications, weather simulations, financial models, and even some biological systems, involve numerous variables that interact in intricate ways. Capturing all these variables in a simulation can be not only computationally intensive but also practically infeasible. This is particularly problematic when real-time decisions are required or when running large-scale simulations over extended periods [14].

This study is based on the recent work by Olofsson et al. [15], where a 3D global CFD model was developed and validated that allowed for making predictions of L_{fill} and RTD based on a given throughput and auger screw rotational speed of a starved fed single-screw extruder system. In this study, however, the considered extrusion system is more complex, having a die plate with over a thousand small cylindrical capillaries. Due to the needed model resolution and resulting calculation times, this would render it unfeasible to be fully resolved in a global CFD model. Therefore, a porous media model was introduced to represent the die plate permeability, reducing the model's degree of freedom while still capturing the correct capillary resistance. Additionally, trace study simulations are already an extremely time-consuming task for generating RTD and RSD based on a global CFD model. With the ambition of utilizing real-time RTD predictions as a metric for process optimization, a reduced order model is required. Therefore, a 2D convection-diffusion finite-difference-based ROM was coupled with the CFD model, allowing RTD predictions with significant speed-up compared to generating RTDs using the CFD model. The basis of the ROM predictions utilizes the fluid velocity field from the global CFD model as model inputs to predict process parameter-specific RTD by calibrating a system-specific diffusion coefficient. The strategy of discretization (binning) of the velocity field to be transferred refers to the previous work by Portillo et al. [16]. This study's input process parameters were throughput and auger rotational speed.

The objective of this work is to establish a numerical simulation procedure allowing for the promotion of L_{fill} and RTD for application in metamodel-based simulation optimization (MBSO) and construction of a system digital twin.

This research introduces a novel approach for understanding starve-fed single-screw extrusion systems in a domain where precision and efficiency are paramount. The essence in the novelty lies in employing advanced numerical 3D simulations to calibrate a 2D-reduced dimensional model (ROM). The implementation of a ROM drastically cuts down computation times from over a week to mere seconds. This efficiency opens doors to many applications, especially those requiring real-time feedback and optimization [17, 18]. The study further sheds light on the intricate fluid-solid interactions, especially the challenges arising from truly representing the quasi-static nature of an industrial extrusion system. This insight paves the way for further research into accurately capturing these interactions in reduced order models.

The remainder of the aper is structured as follows: Section 2 introduces the computational framework and numerical and analytical models with relevant theory. Section 2.2.2 presents and discusses the results, whereas section 3 summarizes the study's main conclusions.

2 Methodology

2.1 System diagram

Figure 1 shows the flow diagram of the coupling framework of the CFD model and the reduced order 2D convection-diffusion model based on a finite difference discretization. Based on a specified throughput (Q) and auger rotational speed (V), a CFD simulation is conducted to approximate L_{fill} for the extruder system. The velocity field is correspondingly mapped onto the finite-difference grid, and a prediction of the RTD is obtained via the convection-diffusion model. The mean residence time (MRT) can further be approximated from the resulting RTD curve.

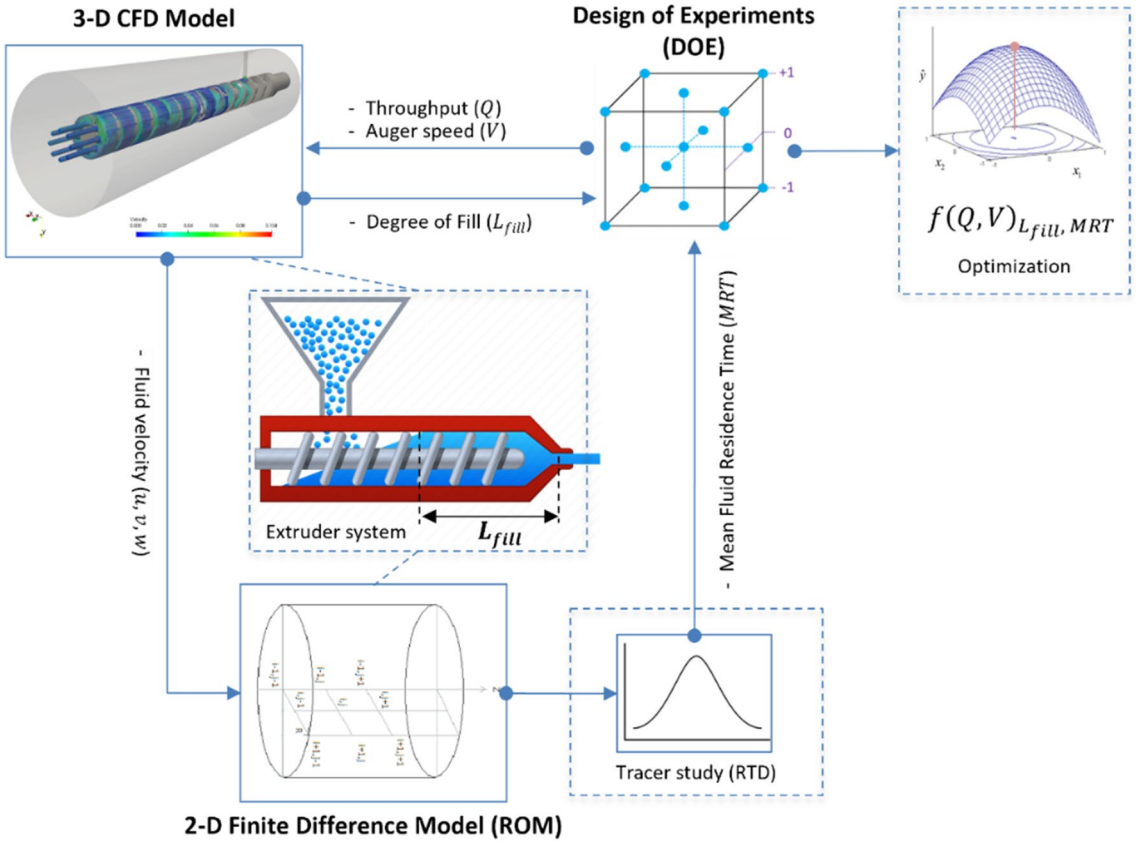

Fig. 1 Schematic visualization of the process of producing a reduced order model (ROM) for predictions of the degree of fill and residence time distribution

The flow diagram additionally shows how a design of experiments (DOE) could lay the basis for globally exploring the parameter space, i.e., producing a simulation-based metamodel that would enable near real-time predictions and process optimization. Hence, multiple design points (DP) would be needed to accurately cover the entire parameter space, and the ROM representation is the enabler for completing the list of DOE design points within a manageable time frame.

The process parameter combinations in this study are based on a twenty-point Latin Hypercube filling design, with three specific design points selected from this experimental setup to represent varying levels of extruder barrel filling: low, medium, and high.

2.2 Numerical modeling

2.2.1 3D Global CFD model

The CFD model is a global 3D model, considering the entire extruder system from inlet to outlet. All simulations consider a laminar, transient, isothermal fluid flow. The material is further assumed to be incompressible, thus implying a constant density.

The numerical problem is solved based on the continuity (Eq. (1)) and momentum (Eq. (2)) equations:

$$\nabla \cdot \boldsymbol{u} = 0 \tag{1}$$

$$\rho\left[\frac{\partial \mathbf{u}}{\partial t} + (\boldsymbol{u} \cdot \nabla)\boldsymbol{u}\right] = -\nabla p + \rho \mathbf{g} - (\nabla \cdot \boldsymbol{\sigma}), \tag{2}$$

where $\boldsymbol{g} = (9.82, 0, 0)$ corresponds to the constant gravitational vector, ρ the density, p the pressure, and $\boldsymbol{\sigma}$ the material deviatoric stress tensor defined as follows:

$$\boldsymbol{\sigma} = 2\mu(\dot{\gamma}, T)\boldsymbol{D} \tag{3}$$

$\boldsymbol{D}$ is further the deformation rate tensor defined as follows:

$$\boldsymbol{D} = \frac{1}{2}\left(\nabla \boldsymbol{u} + (\nabla \boldsymbol{u})^T\right) \tag{4}$$

Simulations were conducted in the commercial CFD software flow 3D [19], where continuity and momentum equations are solved using the finite volume method, and the

free surface position is determined with the volume of fluid technique (VOF) [20]. Viscous stress and pressure are solved implicitly, while the advection equation is solved explicitly with an accuracy of second order.

The considered material is a viscoplastic fluid modeled using a modified Herschel Bulkley model without temperature dependency. The traditional Herschel-Bulkley model, in viscosity format, is given as follows:

$$\mu = \begin{cases} \infty, & for\ \dot{\gamma} \le \dot{\gamma}_c \\ k\dot{\gamma}^{n-1} + \frac{\tau_0}{\dot{\gamma}}, & for\ \dot{\gamma} > \dot{\gamma}_c \end{cases} \quad (5)$$

where τ_0 corresponds to the yield stress, k is the consistency index, n is the flow index, $\dot{\gamma}$ the fluid shear rate, and $\dot{\gamma}_c$ the critical shear rate. Table 1 states the material properties used in the CFD model, which are determined using capillary rheometry based on a manually prepared batch of material [15].

A global mesh sensitivity analysis was conducted to verify a sufficient grid resolution for the numerical model to produce valid results. This was done by comparing the probed extrusion pressure at the quasi-static state at different global mesh resolutions. As seen in Fig. 2, the study indicated that an element with an edge length of 4 mm would be the tradeoff between accuracy and simulation time. This cell size was, therefore, used for all the simulations presented in this study.

Predictions using the CFD model were based on executing simulations in two consecutive steps [15]:

1. In the first step, the model is initiated and simulated until it reaches a quasi-static processing state. Since the extrusion pressure is directly related to the extruder degree of fill, which is further based on a balance between the process parameters (auger speed and throughput), steady state is reached for both pressure and degree of fill. Hence, the model is initiated and executed for each design point until a horizontal global pressure trend is seen. Figure 3 shows a pressure vs. time curve when transitioning from one set of process parameters to another and the plateauing of the monitored pressure at the die plate when returning to stable operating conditions at a different level.

The element-wise fluid fraction ($\boldsymbol{\varphi}$) and velocity components ($\boldsymbol{u_x}, \boldsymbol{u_y}, \boldsymbol{u_z}$) are then exported to a file to allow for subsequent postprocessing, i.e., the calculation of L_{fill} and RTD based on the respective data.

The following summation of the individual element fluid fractions gives the overall fill fraction along the barrel axis:

$$\boldsymbol{F}(z) = \frac{1}{A(z)} \sum_{A(z)} \boldsymbol{\varphi}(x, y) \Delta x \Delta y, \quad (6)$$

where z is the distance from the point under consideration to the inner surface of the die plate. The fill length is now determined as follows:

Table 1 Values for the density and viscosity model

Symbol	Value	Unit
ρ	1404	kg/m^3
k	5861.84	$Pa \cdot s^n$
n	0.212	-
τ_0	1.74e+05	Pa
$\dot{\gamma}_c$	59.34	s^{-1}

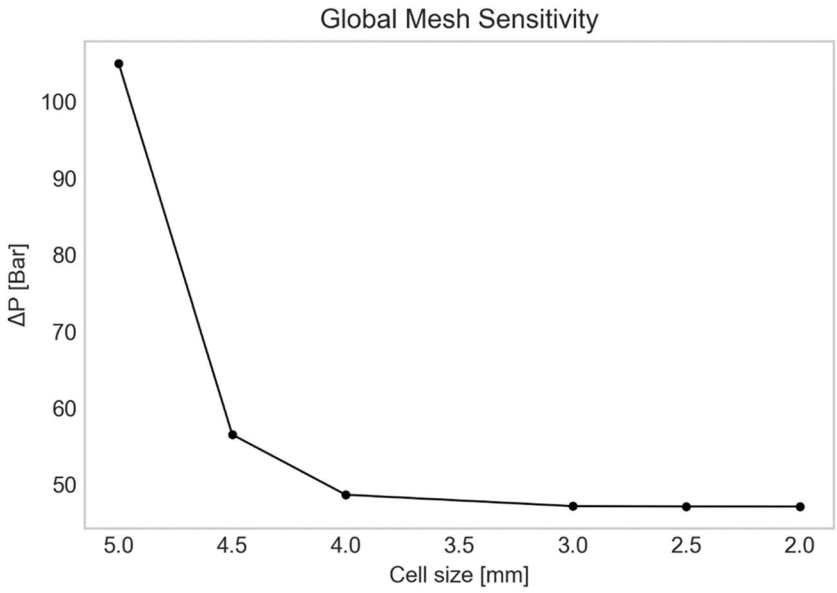

Fig. 2 Extrusion pressure based on different numerical mesh cell sizes

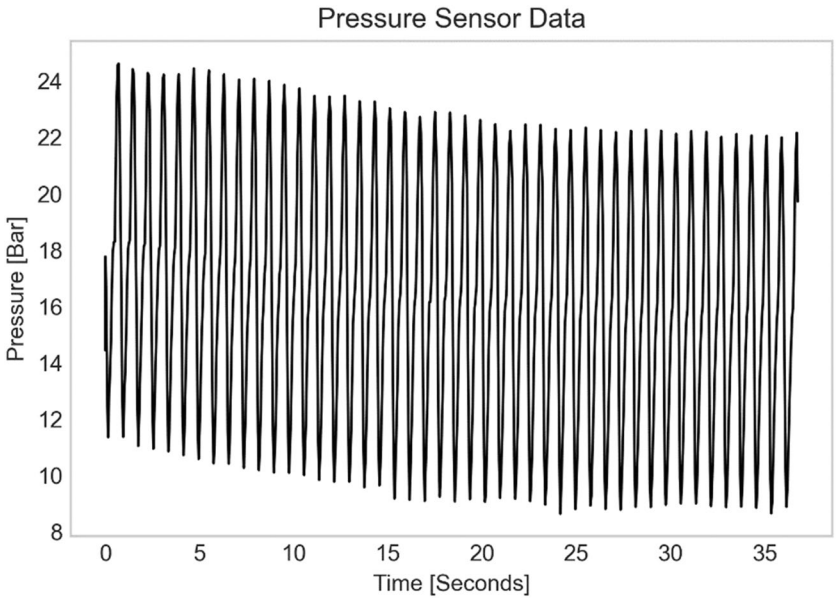

Fig. 3 Pressure monitoring curve from the CFD simulation, where the average pressure converges

$$L_{fill} = \frac{z(F_i \geq 99\%)}{z_L} \begin{cases} where \;\; F_{(i+1)} \geq 99\% \\ and \;\;\; F_{(i-1)} < 99\% \end{cases}, \tag{7}$$

where z_L corresponds to the total length of the extruder barrel and "i" is a counter in the z-direction.

2. In the second step, a trace study simulation is initiated by restarting the model from the last registered time step in the first simulation step. This implies that a tracer (a detectable substance that does not react with the system's contents) is introduced. As the tracer moves through the system, its concentration over time is monitored at a fixed point at the die plate exit. This tracer concentration as a time function is plotted to generate the RTD curve. For this purpose, a fluid scalar assignment was utilized in the CFD software. Scalars are defined as concentration, e.g., amount per volume, and can be assigned to any existing or introduced fluid. A transport equation is subsequently solved for each advectable scalar. For this study, a concentration of 100 kg/m^3 was assigned to a small fluid parcel (0.288 cm^3) being introduced just below the inlet boundary. It should be noted that, except for the scalar concentration definition, the introduced fluid parcel has the same properties as the remainder of the fluid, e.g., density, viscosity, elastic modulus, and viscoelastic properties. The contour shown in Fig. 4 shows a 2D sectional contour plot of the instantaneous spatial distribution of the advected scalar concentration when mixed with the remainder of the processed fluid. The contour corresponds to the scalar mass per open cell volume. The open-cell volume is calculated based on the fluid fractional area-volume obstacle representation (FAVOR^{TM}) method [21], which calculates open cell areas and volumes to define the region within a cell occupied by the obstacle. Thus, the open cell volume refers to the volume occupied by the fluid inside the extruder.

Using four stationary probing points just behind the die plate, the transient scalar concentration data is monitored and exported for further postprocessing to produce a visual representation. The probing points were evenly distributed, e.g., spaced with a 45-degree angle and situated at a

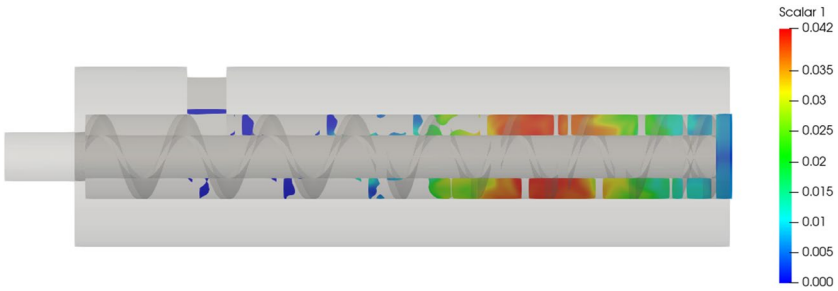

Fig. 4 Scalar concentration distribution [kg/m^3] in the extruder barrel at one time frame during the CFD simulation. Note that the initial scalar concentration has been widely distributed within the extruder

radial distance halfway between the screw root barrel radius (Fig. 5).

The residence-time distribution function for a pulse input is defined as follows:

$$\boldsymbol{E}(t) = \frac{C(t)}{\int_0^\infty C(t)dt} = \frac{C(t)}{\sum_0^\infty C(t)\Delta t} \tag{8}$$

where $C(t)$ represents the given tracer concentration.

Due to the significant difference in the relative size of the die and barrel, modeling the actual dies would require very high mesh resolution and tremendous computational power to reach reasonable calculation times. Therefore, the die plate was modeled as a permeable porous media via a b-grid process in which bulk fluid velocity and pressure drop were calculated according to a given drag model. For this study, the Darcian saturated drag model [22] was used as one of the available models in the CFD software Flow3D. The udirectional flow rate through a porous media can hence be approximated according to the following:

$$\mathbf{u}_{\text{bulk}} = -\frac{K_i}{\mu}\nabla \text{p}, \tag{9}$$

where $\mathbf{u}_{\text{bulk}}$ is the apparent velocity, K_i the intrinsic permeability, μ the dynamic viscosity, and ∇p the pressure gradient of the porous material. The permeability can be expressed in terms of the drag coefficient (F_d) according to the following:

$$F_d = \frac{\phi\mu}{\rho K_i}, \tag{10}$$

wre ϕ corresponds to the porosity of the solid material and ρ the density of the fluid. Based on the Hagen–Poiseuille [23] equation, the flow through a set of capillaries can be defined as follows:

$$Q = \frac{nA\pi r^4 \Delta p}{8\mu L}, \tag{11}$$

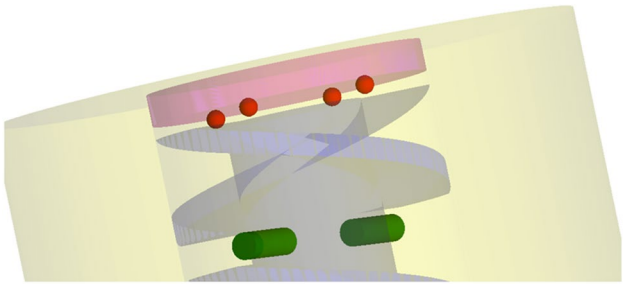

Fig. 5 The placement of probing points for scalar concentration monitoring

where n is the number of capillaries and A and r are the respective cross-sectional area and radius of one capillary. Substituting the integrated form of Darcy's law [24] into Eq. (11), the intrinsic permeability can be derived as follows [25]:

$$K_i = \frac{\phi r^2}{8} \tag{12}$$

The porosity is defined as follows:

$$\phi = \frac{V_P}{V_b}, \tag{13}$$

where V_P and V_b are respective die plate void and bulk volumes. For the considered extruder system die plate, the drag coefficient was calculated to be 2.17e+7 [m^2] and the porosity to 0.11.

2.2.2 2D Convection-diffusion-reduced order model

The general convection-diffusion equation, considering no sources or sinks and a velocity field describing an incompressible flow, is given by the following [26]:

$$\frac{\partial C}{\partial t} = D\nabla^2 C - \text{u} \cdot \text{C}, \tag{14}$$

where C corresponds to a scalar concentration, D the material diffusion coefficient, and u the velocity field that the quantity is moving with.

For a 2D cylindrical system like an extruder, Eq. (14) takes the following form for describing the blending of particulate material [27]:

$$\begin{aligned}&\frac{\partial C(r,z)}{\partial t} + u_r\frac{\partial C(r,z)}{\partial r} + u_z\frac{\partial C(r,z)}{\partial z}\\ &= D\left[\frac{\partial^2(r,z)}{\partial r^2} + \frac{\partial^2(r,z)}{\partial z^2} + \frac{1}{r}\left(\frac{\partial(r,z)}{\partial r}\right)\right]\end{aligned} \tag{15}$$

However, for the residence time distribution (RTD), the radial direction exerts no significant influence on the moments of the RTD or the complete distribution. Thus, the radial diffusion term in equation (15) can be neglected. However, the convective contribution is beheld. This implies that the convection-diffusion representation reduces to the following [16]:

$$\frac{\partial C(r,z)}{\partial t} = D\left[\frac{\partial^2 C(r,z)}{\partial z^2}\right] - u_r\frac{\partial C(r,z)}{\partial r} - u_z\frac{\partial C(r,z)}{\partial z} \tag{16}$$

A finite difference approach was employed to numerically solve the two-dimensional convection-diffusion equation [28–30]. The domain is divided according to $z_1 \le z_i \le z_{M+1} = \text{L}_B$ and $r_1 \le r_j \le r_{N+1} = \text{R}_B$ as seen in Fig. 6.

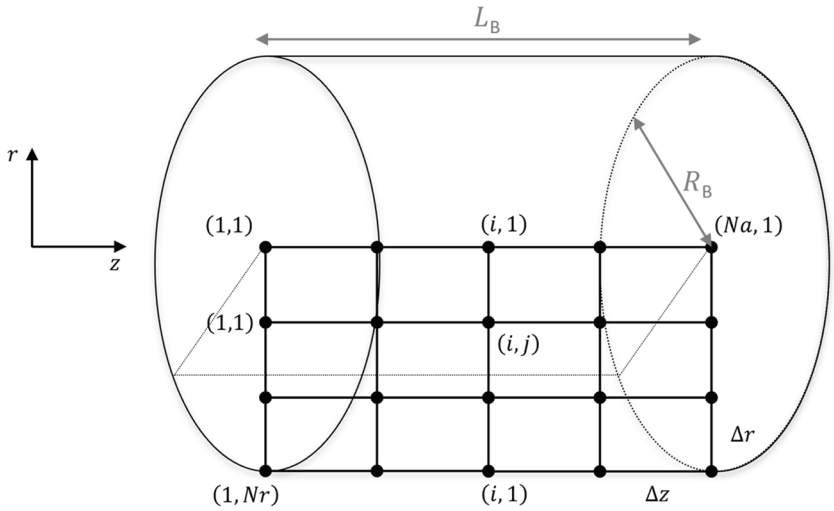

Fig. 6 A 2D barrel discretization for modeling RTD and relative RSD of a pulse injection test

Parameters L_B and R_B correspond to the barrel length and radius. The time is divided into equal steps of size Δt, with time $t_n - n\Delta t$. After discretization of Eq. (16) in space and time, the concentration for each grid point is approximated as follows:

$$C_{i,j}^{t+\Delta t} = C_{i,j}^{t} + \Delta t \left[D\left(\frac{C_{i-1,j}^{t} + C_{i+1,j}^{t} - 2C_{i,j}^{t}}{\Delta z^2} \right) - \left(\frac{u_{z,i} C_{i,j}^{t} - u_{z,i-1} C_{i-1,j}^{t}}{\Delta z} \right) - \left(\frac{u_{r,j} C_{i,j}^{t} - u_{r,j-1} C_{i,j-1}^{t}}{\Delta r} \right) \right] \tag{17}$$

Thus, the numerical scheme is Forward in Time and Centered in Space for diffusion (FTCS) and Forward in Time and Backward in Space for advection (FTBS). The bottom ($y = 0$) and top ($y = R_B$) of the finite-difference grid corresponds dimensionally to the respective root and screw radius. Hence, no fluid flux over these boundaries is to be considered. The scalar concentration at the point of model initialization is distributed on the inlet boundary nodes, corresponding to the same concentration and area ratio as the fluid scalar parcel in the validating CFD simulations.

Cartesian velocity components ($\boldsymbol{u}_x, \boldsymbol{u}_y, \boldsymbol{u}_z$) from the quasi-static CFD model are initially transformed to a cylindrical coordinate system ($\boldsymbol{u}_r, \boldsymbol{u}_\varphi, \boldsymbol{u}_z$). Average velocities then have to be calculated within discrete bins according to Fig. 7.

The calculation of binned velocities in respective directions can mathematically be expressed as follows:

$$u_r(i) = \sum_{dr(i)} \frac{u_r}{N} \tag{18}$$

$$u_z(j) = \sum_{dz(j)} \frac{u_z}{N}, \tag{19}$$

where N corresponds to the number of mesh cells contained within each successive bin. The resulting average binned velocities are finally mapped to their corresponding grid point in the convection-diffusion model, discretized according to Fig. 6. Consequently, radial velocities vary over a finite number of radial bins (Nr) but remain constant in axial direction, and axial velocities vary over a finite number of axial bins (Na) but remain constant in radial direction. Ten bins were used in both radial and axial directions.

As the ROM is limited to two dimensions, the $\boldsymbol{u}_\varphi$ component is accounted for by augmenting the axial component with the angular velocity according to following:

$$u_z = \boldsymbol{u}_z + 2\pi \cdot \delta \cdot R_B \cdot \boldsymbol{u}_\varphi \cdot \tan(\boldsymbol{\beta}), \tag{20}$$

where R_B is the screw radius and $\boldsymbol{\beta}$ is the helix angles of the screw flights for the corresponding bins [31]. Then, δ represents a geometry-specific velocity augmenting factor determined by L_{fill}. The determination was done by, per design point, alignment of the initiation points of RTD curves, i.e., iteratively increasing the factor until perfectly overlapping left tails of RTD curves from both the CFD and the ROM. Equation (8) was used to calculate the residence-time distribution curve at the outlet boundary, which corresponds to all the grid points at location $i = Na$.

Figure 8 shows the finite-difference domain, where the x-axis represents the axial direction of the extruder barrel and the y-axis represents the radial direction. The left boundary, at $x = 0$, represents the barrel inlet, and the right-hand side, at $x = 0.923$ m, represents the outlet of the extruder barrel. During a simulation, a small parcel of scalar material is processed from the inlet to the outlet. The contour represents the scalar concentration over the entire processing domain 330 s after simulation initiation. The probed

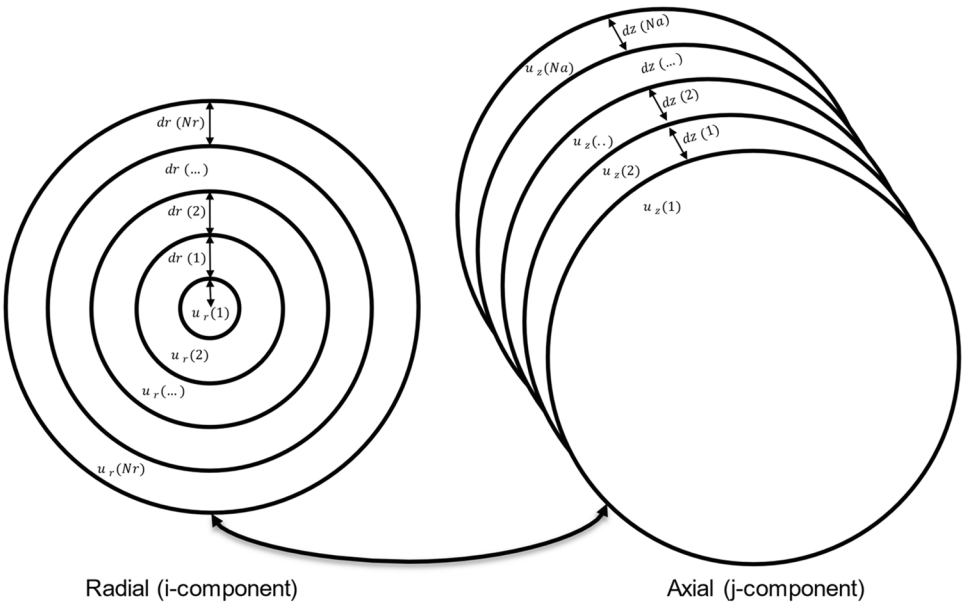

Fig. 7 Average velocities (u_r, u_z) calculated within discrete bins (volumes). ROM grid point velocities are, within corresponding bins, represented by the calculated average velocities according to Eqs. 18 and 19

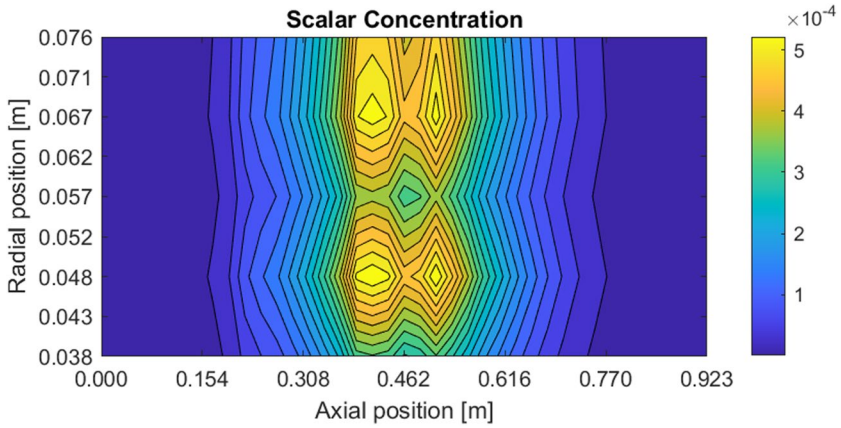

Fig. 8 Scalar concentration distribution in the extruder barrel during one time frame during the ROM simulation

scalar contraction over the outlet boundary constitutes the basis for generating the RTD curves. Figure 8 is, therefore, analogous to Fig. 4. However, it is represented here by a 2D ROM instead of a 3D CFD simulation. The contour in Fig. 8 represents the scalar mass per total grid area.

2.3 Validation and calibration

2.3.1 3D Global CFD model

The CFD model was validated using sensor data from four physical extruders running in parallel. The data set corresponded to 1044 data points, including auger rotational speed, extrusion pressure, and average throughput. In Fig. 9, the distribution of sensor data is visualized via violin plots. They combine elements of a box with a kernel density plot to provide a more comprehensive view of the data's distribution. Inside each violin plot is a miniature box plot, including a median line, quartiles (the 25th and 75th percentiles), and whiskers (representing the data range, excluding outliers). The width of the violin at any given point represents the density of data points at that value. Wider parts indicate higher data density, while narrower parts indicate lower data density.

To investigate the accuracy of the CFD model, a simulated extrusion pressure was compared with the sensor data, where the validation pressure was calculated as the average of median values from all extruders (represented by the white dots in Fig. 9). The simulated auger speed was further calculated as the average of medians from all four extruders, and the simulated throughput was calculated as the median of the average throughput (mass flow).

Auger screw flights exhibit wearing over time, which correspondingly affects the ability to build pressure in the extruder barrel. Therefore, a second validation simulation with an approximated screw wear was also performed. The

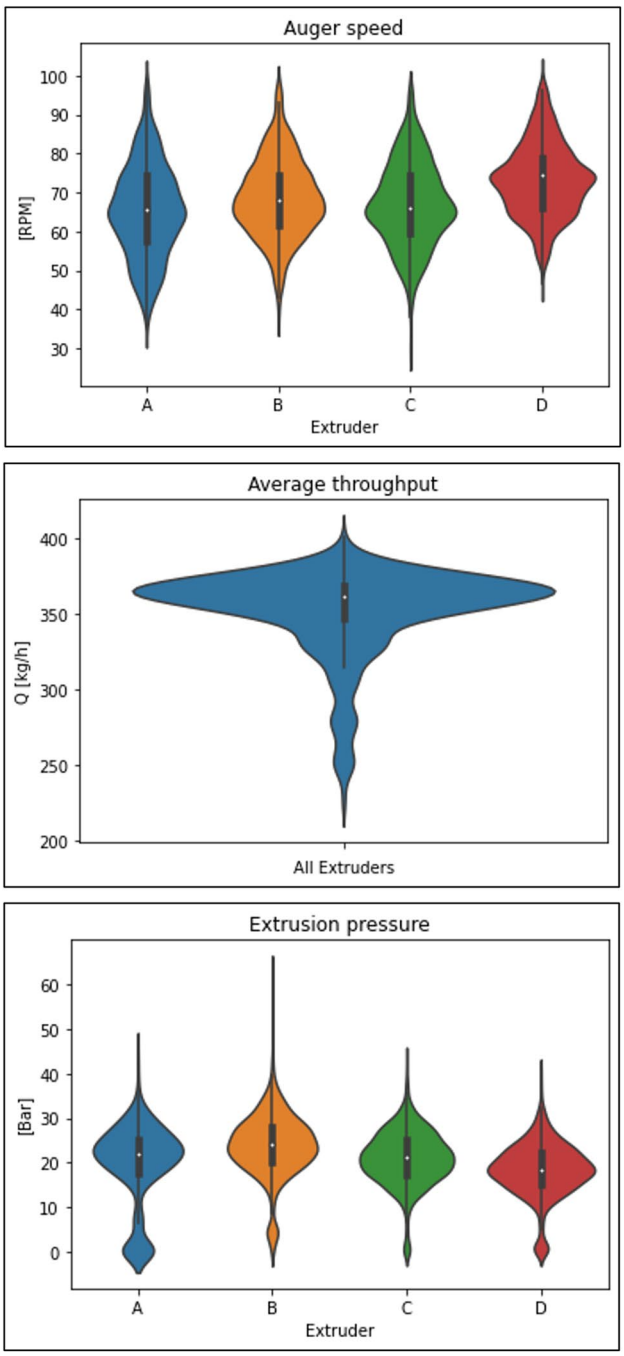

Fig. 9 Violin plots of the production data set corresponding to measured auger speeds, overall throughput, and extrusion pressures.

wear was considered as a radial reduction of the first four screw flights and added to the data set by a linear approximation based on dates when screws were refurbished and a common maximum wear at refurbishing. Refurbishing implies reinstating zero wear on the screw considered wearing flights. The simulated wear gap was finally taken as an average from all extruders over the given period of sensor data sampling. The validation data is stated in Table 2.

Table 2 Validation data and simulation results related to confirming CFD model accuracy

V (data) [RPM]	Q (data) [cm^3/s]	$\Delta P_{val.}$ (data) [Bar]	$\Delta P_{sim.}$ (no wear) [Bar]	$\Delta P_{sim.}$ (with wear) [Bar]	*Wear gap* (approx.) [mm]
68.08	71.46	23.36	26.29	24.89	2.25

2.3.2 2D Reduced order finite-difference model

The calibration of the ROM with respect to the CFD model is carried out by determining the combination of D and δ that minimizes a defined objective function (E_{tot}). The objective function relates to mean residence time (MRT), skewness (γ), and variance (σ^2) of RTD curves according to the following:

$$E_{tot} = E_{MRT} + E_{\sigma^2} + E_{\gamma} \tag{21}$$

The variance is calculated according to the following:

$$\sigma^2 = \int (t-\mu)^2 \cdot \boldsymbol{E}(t)\, dt, \tag{22}$$

where μ is the mean of the distribution, defined as $\mu = \int t \cdot \boldsymbol{E}(t)\, dt$, and $\boldsymbol{E}(t)$ is the residence-time distribution function calculated according to Eq. (8). The skewness is calculated according to the following:

$$\gamma = \frac{\int (t-\mu)^3 \cdot \boldsymbol{E}(t)\, dt}{\sigma^3} \tag{23}$$

Respective errors are calculated as follows:

$$E_{MRT} = \frac{\left|MRT_{curve\ 1} - MRT_{curve\ 2}\right|}{\max\left(MRT_{curve\ 1}, MRT_{curve\ 2}\right)}, \tag{24}$$

$$E_{\sigma^2} = \frac{\left|\sigma^2_{curve\ 1} / \sigma^2_{curve\ 2}\right|}{\max\left(\sigma^2_{curve\ 1}, \sigma^2_{curve\ 2}\right)}, \tag{25}$$

$$E_{\gamma} = \frac{\left|\gamma_{curve\ 1} - \gamma_{curve\ 2}\right|}{\max\left(\gamma_{curve\ 1}, \gamma_{curve\ 2}\right)} \tag{26}$$

Each property plays a role in describing the shape and location of a distribution. The MRT supports the alignment of central location, σ^2 the alignment of spread, and γ the alignment of shape and symmetry.

The diffusion coefficient (D) is determined using the MATLAB *fminsearch* optimization function [32], which is based on the Nelder-Mead simplex algorithm [33], an

iterative optimization technique that does not require the derivative information of the function being minimized. The termination criterion for the optimization algorithm was based on a change in the decision variable (D) below $1e^{-12}$ or reaching 1000 cycles. Hence, the optimizer returns a D based on minimizing E_{tot}.

The determination of δ was based on iterative screening for the overall minimum E_{tot} by incrementing the correction factor by a value of 1e-3. This implies that an optimization of D (*fminsearch* optimization) is performed for each consecutive update of δ. Figure 10 shows the evolution of E_{tot} with changing δ for the first considered design point. The resulting δ is the value that minimizes the E_{tot} curve, with D corresponding to the reported value from the *fminsearch* optimizer at that particular δ.

3 Results and discussn

As previously stated, the simulation was compared with average data from four different production extruders, and the simulated extrusion pressure ($\boldsymbol{\Delta P}_{sim.}$) and extrusion pressure from physical sensors ($\boldsymbol{\Delta P}_{val.}$) can be seen in Table 2.

As compared to the validation pressure, the simulation resulted in a ~11% higher extrusion pressure when considering no screw wearing and only ~6% higher when including an approximated screw wear gap in the simulation. This accuracy was considered satisfying with respect to potential errors relating to data averaging, data quality, and numerical modeling approximations and limitations. It was further noticeable that advection accuracy in the fluid momentum equations needed to be second-order accurate in space, to dynamically capture the transitioning of the free-surface position. Because when initially testing with first-order accuracy only, the experience was that the free surface transition became highly sensitive, coarse and for some situations even unphysical, when adjusting process parameters.

Figure 11 shows the CFD results representing the fill fraction as a function of the normalized axial coordinate of the extruded barrel for three considered trace study design points (DP). The L_{fill} value stated in Table 3 corresponds to the point at where the fill fraction reaches 1.0. Distinct fluctuations in the unfilled section are mainly defined by flow disturbance around the barrel mixing pins [15].

Calculation times for the respective simulation models are further stated in Table 3, where CFD_t represents the simulation time for the CFD model and ROM_t the simulation time for the ROM model. The table further represents the process and information flow from left to right with considerations to each simulation step, i.e., for each consecutive design point, screw rotational velocity (V) and throughput (Q) initially make the basis for the first CFD simulation (step 1). This simulation generates L_{fill} and a quasi-static velocity field ($\boldsymbol{u}$). With reference to this velocity field, trace simulations are conducted with respective CFD (Step 2) and ROM (Step 3) models.

The main goal with a ROM model is to get comparable results as from a more high-fidelity model, however much faster. Moreover, this is very much the case here, as Table 3 shows that trace simulation times go from just over a week using CFD (Step 2) to a couple of seconds when using the ROM (Step 3). It can further be noted that the calculation times have an opposite trend with respect to the level of fill, which is mainly due to the increased level of fluid free surface and distributive mixing when the level of fill decreases. The increased presence of rapidly changing interfaces or sudden changes in flow conditions requires smaller numerical time steps for stability and accuracy, directly related to

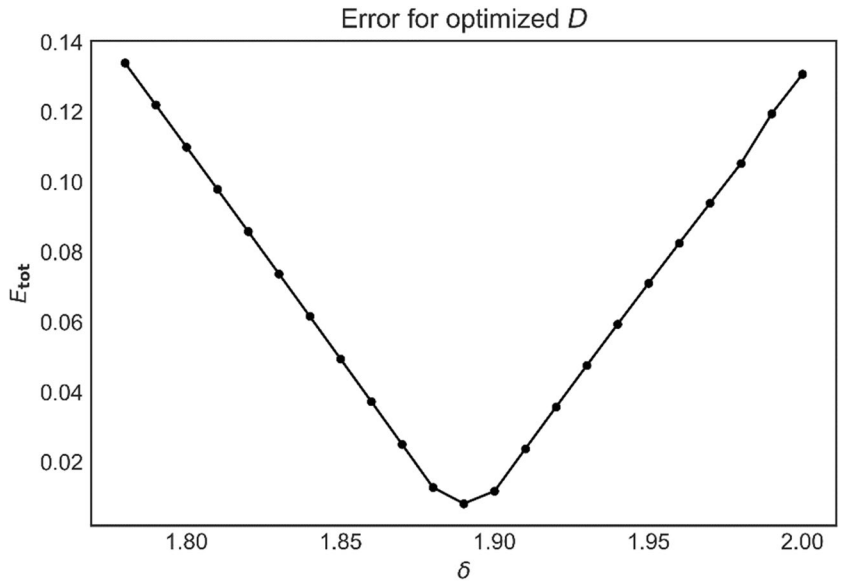

Fig. 10 Evolution of E_{tot} when incrementing the correction factor (δ)

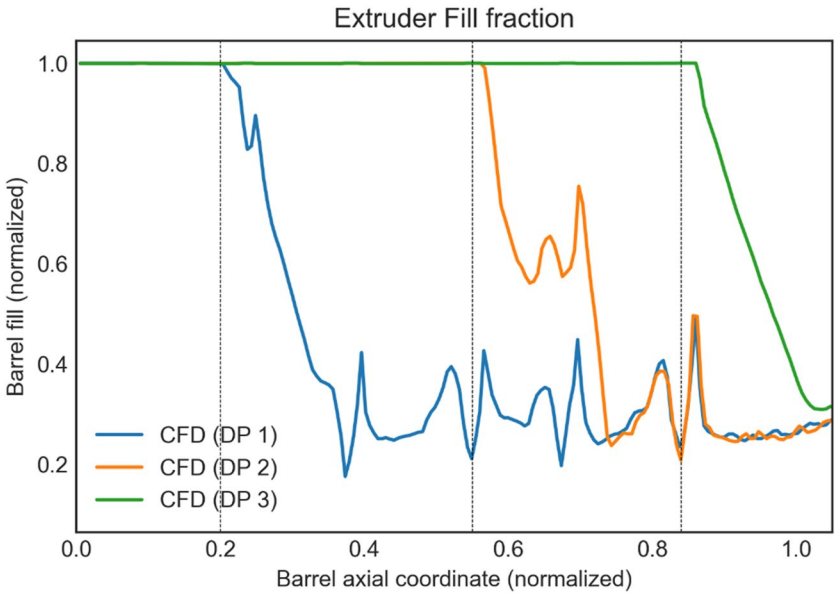

Fig. 11 Normalized fill fraction against normalized extruder barrel axial position

Table 3 Simulation times of respective CFD and ROM models. Step 1 data corresponds to the generation of a quasi-static velocity field with the CFD model. Step 2 data corresponds to running a trace study simulation with the CFD model. Step 3 corresponds to running a trace study simulation with the ROM model

DP			Step 1			Step 2		Step 3	
	V	Q	CFD_t	L_{fill}	$\overset{u}{\Rightarrow}$	CFD_t	$\overset{RTD}{\Rightarrow}$	ROM_t	$\overset{RTD}{\Rightarrow}$
	[*RPM*]	[cm^3/s]	[*hr*]			[*hr*]		[*s*]	
1	74.24	71.27	13.19	0.24		215.48		6.43	
2	69.77	71.04	15.22	0.85		209.62		4.84	
3	60.85	70.81	12.24	0.56		165.68		4.40	

resultant simulation times. Each CFD simulation was executed based on 20 computer nodes, and utilizing more computer power would slightly lower simulation times. However, even if increasing the number of computing cores substantially, it would not be possible to produce simulation times remotely near those of the ROM. Furthermore, considering the calculation times, it would be highly time-consuming to base larger experimental designs on the CFD model results. This clearly emphasizes the necessity of utilizing a ROM when considering corresponding results in experimental designs or MBSO, where each design point could be based on only simulation Steps 1 and 3, drastically reducing calculation times.

Figure 12 shows the three obtained axial velocity correction factors δ and a function corresponding to a second order polynomial fit based on them. Referenced factors in the figure are further stated as numerical values in Table 4.

Figure 13 visualizes the RTD curves generated by the CFD (solid) and ROM (dashed) models. In the left-most sub-figure, every ROM prediction considers an individually optimized diffusion coefficient (D_{opt}). In the right-most sub-figure, the ROM predictions consider a common diffusion coefficient (D_{ave}) calculated as the mean of all individually optimized diffusion coefficients.

Even though there is a slight difference between RTDs from respective models, the curves are pretty well aligned. Not including skewness and variance in the objective function for the optimizer will naturally favor better alignment of curve amplitudes. However, this comes with the compromise of a poorer alignment of curve tails and inflection points.

The best fit is produced at design point 3, whereas the accuracy decreases with decreasing level of fill. In general terms, this can be related to the two distinct flow regimes in the extruder. In the fully filled part, the flow is mainly in the direction parallel to the axis of the extruder barrel, a simple "laminar" flow [34] from an overall viewpoint. However, a more complex cross-channel flow occurs in the unfilled section [35]. With the significant amounts of free-surface flow, maintaining the accuracy of the flow prediction becomes inherently more challenging. Hence, as the level of

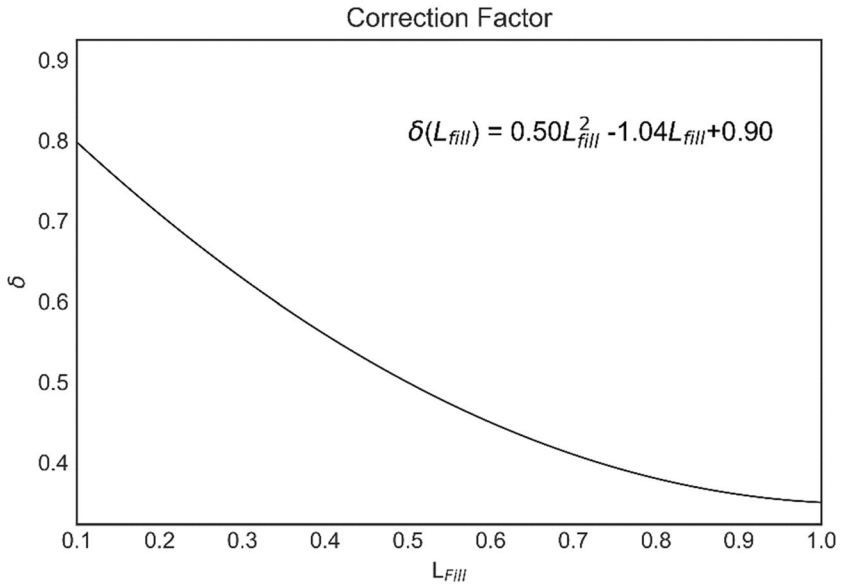

Fig. 12 Correction factors with a fitted second-order polynomial

Table 4 Mean residence time (MRT) from CFD and ROM trace studies

DP	δ	E_{tot}	R^2	*RMSE* [s^{-1}]	L_{fill}	MRT_{CFD} [s]	$MRT_{ROM}(D_{ave})$ [s]	$MRT_{ROM}(D_{opt})$ [s]	D_{opt} [m^2/s]
1	1.89	8.20e-3	0.89	1.14e-3	0.2	121.49	123.39	122.28	3.06e-04
2	1.25	7.08e-2	7.8e-3	3.22e-3	0.56	146.90	135.23	136.55	3.11e-04
3	0.99	2.38e-2	0.77	1.29e-3	0.84	168.64	166.64	168.04	2.30e-04

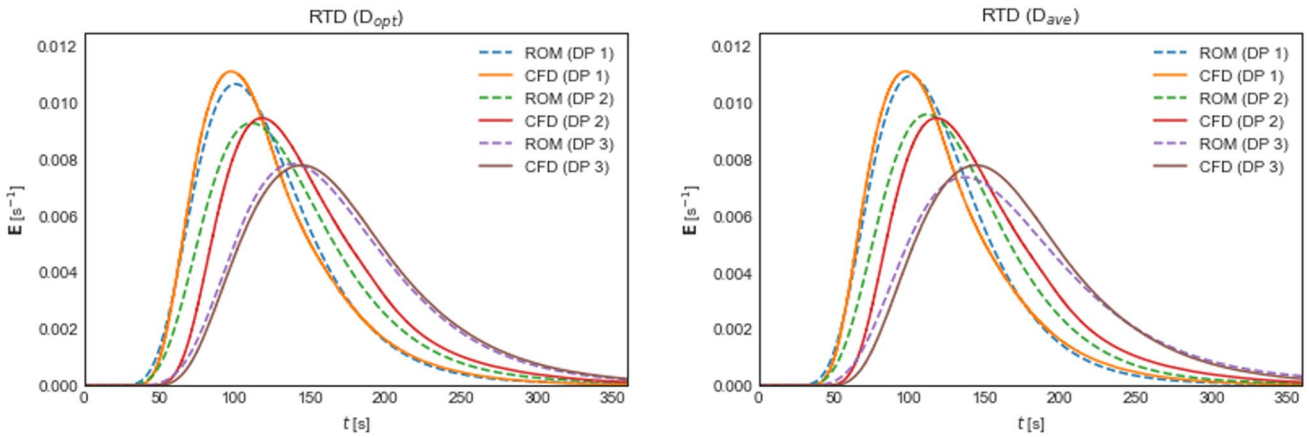

Fig. 13 RTD curves from respective CFD and ROM simulations. Left: ROM curves based on D_{opt}. Right: ROM curves based on D_{ave}

fill decreases, the prediction accuracy decreases correspondingly. A higher-resolution grid could potentially alleviate some of the lost accuracy. However, this would come with a cost of calculation times that would render the proposed methodology unfeasible [36], [20].

The discrepancy between models is further considered to be related to some of the physics being lost during model transition. When considering fluid flow in pipes, it is essential to account for not only axial velocities but also angular and radial velocities. This ensures that the continuity equation is preserved, i.e., that mass is conserved as fluid moves through the pipe in these three velocity components. The objective of Eq. (20) is to convert angular velocities into axial velocities, still preserving mass conservation to the greatest extent achievable. The originally considered equation refers to a constant radial distribution of fluid in relation to the screw helix angle. However, for a partially filled screw, the radial distribution of fluid will vary with the axial

distribution of fill. This is further complicated by biased distributed mixing pins and the screw having a double winding of flights before the front plate die. This is seen as the main reason for the increasing rotational to axial dependency with the degree of fill and the basis for the necessity to establish an augmenting δ factor. The diffusion is further somewhat spatially varying due to pressure and viscosity gradients [37] within the flow domain. Another source of error can be related to the fact that the extruder is not perfectly axisymmetric due to the mixing pins and thereby introducing a weak transient component in the considered quasi-static operational state with auger screw rotations. This is further considered the leading cause of the local fluctuations seen in the extrusion pressure vs. time curve in Fig. 3. The corresponding mean residence time (MRT) for the RTD curves in Fig. 13 is stated in Table 4.

Table 4 further includes evaluation metrics related to the alignment of the computed RTD curves, specifically E_{tot}, $RMSE$, and R^2. The optimized diffusion coefficient varies slightly between design points with an opposite, increasing trend with respect to L_{fill}. However, as a result, the predictions based on a common average diffusion coefficient actually improve the overall alignment of curves. However, differences are not substantial since the deviation in the accumulated error (deviation from CFD) is around 1 s. The best MRT fit for the last design point is achieved considering the roughly half-filled screw. This underlines the complexity of the underlying dynamics and the difficulty of accurately capturing the trend at lower fill levels. Generating additional RTD data, based on a set of process parameters, would correspond to the following:

1. Step 1 is based on specified auger speed and throughput.
2. Calculate the correction factor based on the equation given in Fig. 12.
3. Step 3 with calculated $\boldsymbol{\delta}$ and $D_{ave} = 2.82\text{e-}04$.

All velocities used for respective ROM simulations are given in Table 5 in the Appendix.

4 Conclusions and future works

This study presented a novel approach to modeling an industrial starve-fed single-screw extrusion system, leveraging a comprehensive computational framework that coupled a 3D CFD model with a 2D reduced order convection-diffusion model. The validation of the 3D Global CFD model showed a close alignment with sensor data from physical extruders. Notably, when accounting for partial wear on auger screw flights, the simulated extrusion pressures were within ~6% of validation pressures, stressing the model's strength.

The CFD results, visualized in Fig. 8, offered insights into the system fill fraction as a function of the normalized axial coordinate of the extruder barrel, shedding light on the intricate flow behavior within the system and the transition point, where the latter refers to the evaluation of the fill length (L_{fill}). Furthermore, the quasi-static fluid velocity field mapped from the visualized partially filled CFD model states, provided the basis for sequential trace studies to generate system residence time distribution (RTD) curves, which can be effectively used in design of experiments and building response surface equations for global process parameter optimization and digital twin systems. It could further provide valuable insights with respect to heat transfer, stresses, and characterization of mixing in the extruder.

The 2D convection-diffusion-based reduced order model (ROM) demonstrated its potential by obtaining RTD curves very close to those obtained from the much more comprehensive CFD model (see Fig. 9). Calibration was achieved based on an iterative optimization technique, where a process parameter-specific diffusion coefficient was iteratively modified to achieve the best possible alignment of the ROM. A closer look at the RTD curves, however, indicates that while the ROM is efficient, it still exhibits certain discrepancies when compared to the CFD model. The arrival of the initial tracer scalar was predicted to occur slightly sooner in the ROM. This, coupled with other observed differences, underscores the complexities in transitioning from a detailed

Table 5 Binned velocity data (v_r, v_φ, v_z) from the 3-D CFD model that was used in ROM simulations

Bin	$v_{\varphi,1}$	$v_{r,1}$	$v_{z,1}$	$v_{\varphi,2}$	$v_{r,2}$	$v_{z,2}$	$v_{\varphi,5}$	$v_{r,5}$	$v_{z,5}$
1	6.88E-02	-4.58E-04	2.65E-03	1.01E-01	-5.90E-04	2.97E-03	9.95E-02	-1.37E-03	2.52E-03
2	6.61E-03	-6.00E-09	3.69E-02	8.25E-02	2.85E-08	3.11E-02	8.88E-02	-8.81E-09	3.13E-02
3	1.06E-03	-1.56E-04	2.83E-03	1.26E-01	9.84E-09	2.13E-02	1.42E-01	1.11E-04	2.29E-02
4	7.76E-02	-9.85E-10	2.42E-02	8.86E-02	-2.88E-03	2.25E-03	1.00E-01	3.76E-05	1.48E-04
5	1.05E-01	-2.09E-04	1.75E-02	1.18E-01	-2.64E-03	2.04E-02	1.35E-01	-6.65E-09	1.41E-02
6	9.64E-02	-2.70E-05	1.98E-02	1.20E-02	7.56E-04	1.48E-02	1.37E-01	-1.62E-08	1.38E-02
7	6.45E-02	-1.09E-04	1.55E-02	9.26E-02	-3.56E-03	1.32E-02	1.05E-02	-2.00E-04	1.59E-02
8	9.24E-02	5.76E-05	1.76E-03	1.37E-01	2.19E-08	1.19E-02	1.49E-01	8.11E-09	1.50E-02
9	6.56E-02	3.04E-05	6.16E-03	9.23E-02	2.69E-04	1.04E-02	8.60E-02	1.40E-03	1.26E-02
10	7.29E-02	-4.55E-04	6.40E-03	1.05E-01	-1.88E-03	9.71E-03	9.86E-02	-3.60E-03	1.13E-02

CFD model to a ROM. The challenges stem from nuances such as the quasi-static nature of the CFD simulation and the intricate fluid-solid interactions inherent in the process.

In essence, this research provides a promising avenue for predicting fill-level and residence time distribution in industrial starve-fed single-screw extrusion systems based on reduced order modeling. As industries move towards more agile and data-driven operations, the model's accuracy suggests its potential application in real-time prediction and process optimization in extrusion systems. Future work might delve deeper into refining these models, improving model coupling and scalability, and potentially integrating them into industry-ready software solutions.

Appendix

Author contribution All authors contributed to the study conception and design. Material preparation, data collection, and analysis were performed by E.H.O. The first draft of the manuscript was written by E.H.O., and all authors commented on previous versions of the manuscript. All authors read and approved the final manuscript.

Funding Open access funding provided by Technical University of Denmark

Declarations

Competing interests The authors declare no competing interests.

References

1. Händle F (2019) The Art of Ceramic Extrusion, vol 2019, 1st edn. Springer International Publishing : Imprint: Springer, Cham
2. Giles HF, Wagner JR, Mount EM (2005) Extrusion: the definitive processing guide and handbook. William Andrew Pub, Norwich, NY
3. Mudalamane R, Bigio DI (2004) Experimental characterization of fill length behavior in extruders. Polym Eng Sci 44:557–563. https://doi.org/10.1002/pen.20050
4. Wilczyński K, Nastaj A, Lewandowski A et al (2019) Fundamentals of global modeling for polymer extrusion. Polymers 11:2106. https://doi.org/10.3390/polym11122106
5. Singh B, Rizvi SSH (1998) Residence time distribution (RTD) and goodness of mixing (GM) during CO_2 -injection in twin-screw extrusion part II: GM studies. J Food Process Engineering 21:111–126. https://doi.org/10.1111/j.1745-4530.1998.tb00443.x
6. Zhuang Y, Saadatkhah N, Morgani MS et al (2023) Experimental methods in chemical engineering: reactive extrusion. Can J Chem Eng 101:59–77. https://doi.org/10.1002/cjce.24538
7. Gao Y, Muzzio FJ, Ierapetritou MG (2012) A review of the residence time distribution (RTD) applications in solid unit operations. Powder Technol 228:416–423. https://doi.org/10.1016/j.powtec.2012.05.060
8. Fogler HS (2006) Elements of Chemical Reaction Engineering, 4th edn. Prentice Hall PTR, Upper Saddle River, NJ
9. Emady HN, Wittman M, Koynov S et al (2015) A simple color concentration measurement technique for powders. Powder Technol 286:392–400. https://doi.org/10.1016/j.powtec.2015.07.050
10. Lepschi A, Gerstorfer G, Miethlinger J (2015) Determining the residence time distribution of various screw elements in a co-rotating twin-screw extruder by means of fluorescence spectroscopy. Cleveland, Ohio, USA, p 020005
11. Li G, Mukhopadhyay A, Cheng C-Y, Dai Y (2010) Various approaches to compute fluid residence time in mixing systems. In: ASME 2010. In: 3rd Joint US-European Fluids Engineering Summer Meeting: Volume 1, Symposia – Parts A, B, and C. ASMEDC, Montreal, Quebec, Canada, pp 295–304
12. Schilders WHA, van der Vorst HA, Rommes J (2008) Model order reduction: theory, research aspects and applications. Springer, Berlin
13. Benner P, Grivet-Talocia S, Quarteroni A et al (2021) Model order reduction. De Gruyter, Berlin ; Boston
14. Lassila T, Manzoni A, Quarteroni A, Rozza G (2014) Model order reduction in fluid dynamics: challenges and perspectives. In: Quarteroni A, Rozza G (eds) Reduced Order Methods for Modeling and Computational Reduction. Springer International Publishing, Cham, pp 235–273
15. Olofsson EH, Roland M, Spangenberg J et al (2023) A CFD model with free surface tracking: predicting fill level and residence time in a starve-fed single-screw extruder. Int J Adv Manuf Technol 126(7-8):3579–3591. https://doi.org/10.1007/s00170-023-11329-w
16. Portillo PM, Muzzio FJ, Ierapetritou MG (2008) Using compartment modeling to investigate mixing behavior of a continuous mixer. J Pharm Innov 3:161–174. https://doi.org/10.1007/s12247-008-9036-0
17. do Amaral JVS, de Carvalho Miranda R, JAB M et al (2022) Metamodeling-based simulation optimization in manufacturing problems: a comparative study. Int J Adv Manuf Technol 120:5205–5224. https://doi.org/10.1007/s00170-022-09072-9
18. Barbara R, Lorenzo D, Luca T (2017) Multi-goal optimization of industrial extrusion dies by means of meta-models. Int J Adv Manuf Technol 88:3281–3293. https://doi.org/10.1007/s00170-016-9009-2
19. FLOW-3D (Version 2022R1). Flow Science Inc., Santa Fe, NM, USA. Avaliable at https://www.flow3d.com/products/flow-3d/
20. Hirt CW, Nichols BD (1981) Volume of fluid (VOF) method for the dynamics of free boundaries. J Comput Phys 39:201–225. https://doi.org/10.1016/0021-9991(81)90145-5
21. CFD-101. In: FAVOR™ vs. body-fitted coordinates. https://www.flow3d.com/resources/cfd-101/modeling-techniques/favor-vs-body-fitted-coordinates/

22. Liu M, Suo S, Wu J et al (2019) Tailoring porous media for controllable capillary flow. J Colloid Interface Sci 539:379–387. https://doi.org/10.1016/j.jcis.2018.12.068
23. Ostadfar A (2016) Fluid mechanics and biofluids principles. Biofluid Mechanics. Elsevier, In, pp 1–60
24. Dake LP (1978) Fundamentals of reservoir engineering. Elsevier, Amsterdam London New York [etc.]
25. Al-Doury MMI (2010) A discussion about hydraulic permeability and permeability. Pet Sci Technol 28:1740–1749. https://doi.org/10.1080/10916460903261715
26. Stocker T (2011) Introduction to climate modelling. Springer, New York
27. Johanson K, Eckert C, Ghose D et al (2005) Quantitative measurement of particle segregation mechanisms. Powder Technol 159:1–12. https://doi.org/10.1016/j.powtec.2005.06.003
28. Smith GD (1985) Numerical solution of partial differential equations: finite difference methods, 3rd edn. Clarendon Press ; Oxford University Press, Oxford [Oxfordshire], New York
29. Popescu I (2014) Computational hydraulics: numerical methods and modelling. 1. publ. IWA Publ, London
30. Sepehrnoori K, Carey G, Knapp R (1979) Convection–diffusion computations. In: Kabaila A (ed) Proceedings Intl. Conf. on Finite Element Methods in Engineering. Clarendon Press, Sydney, Australia, pp 345–352
31. Sandu S, Biboulet N, Nelias D, Abevi F (2018) An efficient method for analyzing the roller screw thread geometry. Mech Mach Theory 126:243–264. https://doi.org/10.1016/j.mechmachtheory.2018.04.004
32. (2023) MATLAB Help Center. https://www.mathworks.com/help/matlab/ref/fminsearch.html
33. Lagarias JC, Reeds JA, Wright MH, Wright PE (1998) Convergence properties of the Nelder-Mead simplex method in low dimensions. SIAM J Optim 9:112–147. https://doi.org/10.1137/S1052623496303470
34. Willis AP (2017) The Openpipeflow Navier–Stokes solver. SoftwareX 6:124–127. https://doi.org/10.1016/j.softx.2017.05.003
35. Singh B, Sharma C, Sharma S (2017) Fundamentals of extrusion processing. In: novel food processing technologies. Nanda, V. & Sharma, S. New India Publishing Agency, New Delhi. pp 1–46
36. Ketabdari MJ (2016) Free surface flow simulation using VOF method. In: Lopez-Ruiz R (ed) Numerical Simulation. IntechOpen, Rijeka
37. Costigliola L, Heyes DM, Schrøder TB, Dyre JC (2019) Revisiting the Stokes-Einstein relation without a hydrodynamic diameter. J Chem Phys 150:021101. https://doi.org/10.1063/1.5080662